Extended Metasurface Spin Functionalities from Rotation of Elements

Minggui Wei, Yuhong Xu, Guigeng Liu, Tong Wu, Wanyin Liu, Xiaoqiang Su, Quan Xu, Xueqian Zhang, Jiaguang Han,* Jianqiang Gu,* and Baile Zhang*

Metasurfaces are a class of planar optical components that are engineered to manipulate electromagnetic waves, including their spin states in terms of circular polarizations. For example, the Pancharatnam–Berry (PB) phase has been exploited in metasurfaces for various spin functionalities, but these spin functionalities, exhibit conjugate relations for spin states. Recent advances combining the PB phase and propagation phase have implemented completely independent spin functionalities for spin states. However, the spin functionalities are fixed once the metasurfaces are designed. Here, this work proposes and demonstrates that the spin functionalities designed from the PB phase and propagation phase can be further extended by simply rotating the elements in a metasurface. This extension is based on a relationship between phase profiles of spin states that are acquired before and after the rotation. Proof-of-concept demonstrations are performed for the extended spin functionalities, including the conversion from spin angular momentum to orbital angular momentum, and spin-dependent holograms. This extension may find use in relevant applications such as polarized display and dual-polarized holography.

1. Introduction

Metasurfaces, which consist of subwavelength photonic elements patterned on a flat surface, have provided unprecedented control over electromagnetic waves[1–7] For example, the Pancharatnam–Berry (PB) metasurfaces are able to impart equal but opposite phase profiles to the two spin states by encoding a geometrical PB phase in the orientation angle of the constituent elements, resulting in conjugate spin functionalities.[8–13] The two spin states, namely, the left-handedness circular polarization (LCP) and right-handedness circular polarization (RCP), can be deflected into different directions in a PB metasurface, but these deflection functionalities are unchangeable once the metasurface design is completed. Some metasurfaces are able to tune their spin functionalities,[14–17] as in the previously demonstrated pumping-induced nonlinear deflection[18] and holograms[19] as well as electrically[20–23] or thermally[24,25] modified functionalities. These extended spin functionalities are achieved by engineering the phase response of individual elements in a metasurface. However, such nonlinear tuning so far has not been able to realize continuous phase tuning for the extended spin functionalities.

Rotating elements' orientations can impart continuous phase profiles to spin states, thus being able to extend spin functionalities with more flexibilities.[26] It should be pointed out that in PB metasurfaces, the rotation of elements' orientations will always lead to conjugate spin functionalities for the two spin states, while usually only one of them is of interest in practice. In other words, one of the spin states is sacrificed. Recent studies have shown that by combining the propagation phase and PB phase, it is possible to construct completely independent phase profiles for the two spin states, exhibiting spin-decoupled functionalities.[27–30] Therefore, it is promising

M. Wei, G. Liu, B. Zhang
Division of Physics and Applied Physics
School of Physical and Mathematical Sciences
Nanyang Technological University
21 Nanyang Link, Singapore 637371, Singapore
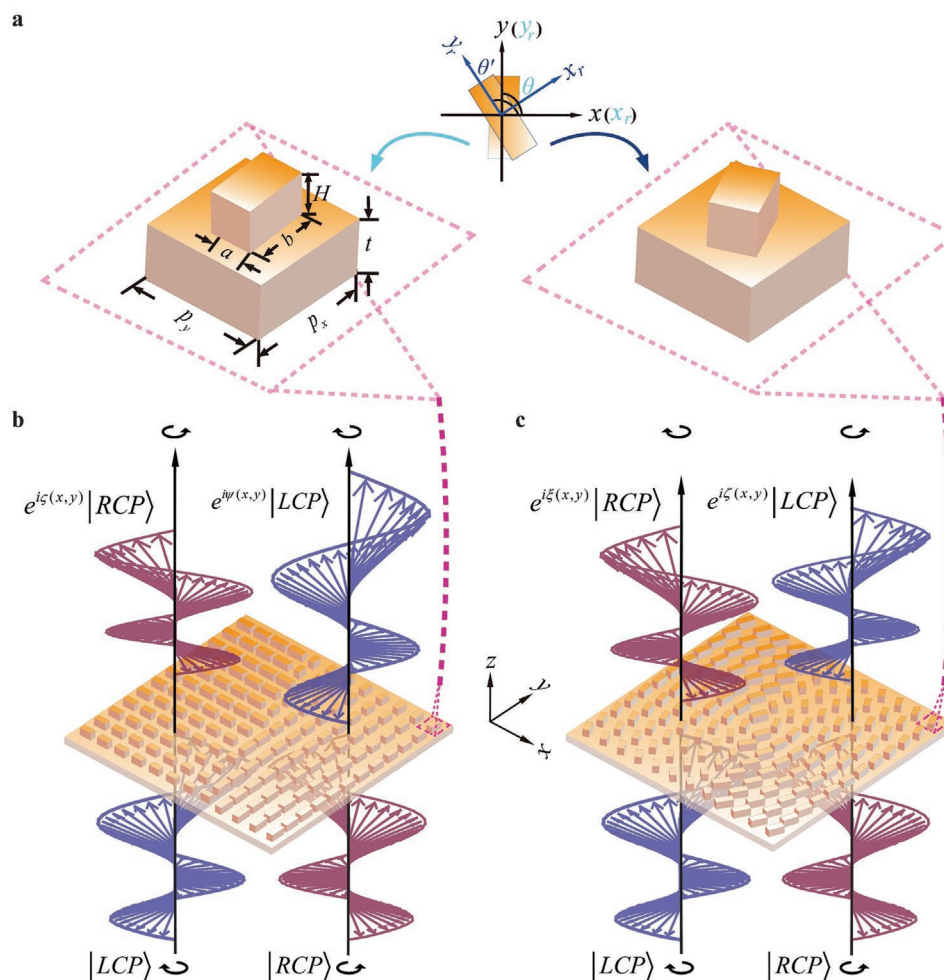E-mail: blzhang@ntu.edu.sg
Y. Xu, T. Wu, W. Liu, Q. Xu, X. Zhang, J. Han, J. Gu
Center for Terahertz Waves and College of Precision Instrument
and Optoelectronics Engineering
The Key Laboratory of Optoelectronics Information and Technology
Ministry of Education
Tianjin University
Tianjin 300072, China
E-mail: jiaghan@tju.edu.cn; gjq@tju.edu.cn

X. Su
Institute of Solid State Physics and College of Physics and Electronic
Science
Shanxi Province Key Laboratory of Microstructure Electromagnetic
Functional Materials
Shanxi Datong University
Datong 037009, China

B. Zhang
Centre for Disruptive Photonic Technologies
The Photonics Institute
Nanyang Technological University
50 Nanyang Avenue, Singapore 639798, Singapore

**ADVANCED
SCIENCE NEWS**
www.advancedsciencenews.com

**ADVANCED
OPTICAL
MATERIALS**
www.advopticalmat.de

Figure 1. Schematic of extended metasurface spin functionalities from rotation of elements. a) Rotation of one element. The element has a length of a, width of b, height H, and t is the thickness of the substrate. The x and y axes are the global axes. The x_r and y_r axes correspond to the fast and slow axes of the element, respectively. The orientation angle is defined as the angle between the y_r axis and the y axis. Here, θ represents the orientation of the element labeled by a red dotted box in (b) ($\theta = \pi/2$ in the illustration), while θ' corresponds to the same element in (c) but with different orientation. b) Schematic of a metasurface with orientation angle distribution $\theta(x, y)$. The incident $|LCP\rangle$ or $|RCP\rangle$ flips the handedness, resulting in $e^{i\varsigma(x,y)}|RCP\rangle$ or $e^{i\psi(x,y)}|LCP\rangle$, respectively. c) Schematic of the metasurface after the rotation of elements to exhibit another distribution $\theta'(x, y)$. The incident $|LCP\rangle$ or $|RCP\rangle$ is mapped to $e^{i\xi(x,y)}|RCP\rangle$ or $e^{i\zeta(x,y)}|LCP\rangle$, respectively.

to extend the spin functionalities of a metasurface for the two spin states separately.

Here, we experimentally demonstrate the separate extension of spin functionalities for the two spin states by rotating the elements in a metasurface. The relationship between the phase profiles of spin states before and after the rotation is revealed. The conversion from spin angular momentum to different orbital angular momentum is captured by a terahertz scanning microscope. Extended spin functionalities in terms of spin-dependent holograms are also demonstrated to project different images before and after the rotation. Such extended spin functionalities for different spins may find use in relevant applications such as dual-polarized optical devices.

2. Results and Discussion

Figure 1 shows the conceptual illustration of rotation-extended spin functionalities in a metasurface. As shown in Figure 1a,

a dielectric pillar stands on a substrate, forming a basic element in the metasurface. The dielectric pillar has a length a, a width b and a height H, and t is the thickness of the substrate. The period of elements along the x and y axes are p_x and p_y, respectively. Each element possesses a fast axis and a slow axis, as denoted by x_r and y_r. The orientation angle θ is defined as the angle between the y_r axis of the element and the y axis, as shown in the upper panel of Figure 1a. After rotating the elements, the orientation angle changes from θ to θ', and the overall metasurface reconfigures from Figure 1b,c. Given a fixed incident spin state (either $|LCP\rangle$ or $|RCP\rangle$), the metasurface in Figure 1b will be able to generate an opposite spin state at the output with an additional phase profile. Here, we denote the output spin state as $e^{i\varsigma(x,y)}|RCP\rangle$ or $e^{i\psi(x,y)}|LCP\rangle$), where $\varsigma(x, y)$ and $\psi(x, y)$ are the corresponding phase profiles for different spins. In contrast, the output spin state from the metasurface in Figure 1c will have a different phase profile, $\xi(x, y)$ and $\zeta(x, y)$, such as the output spin state can be denoted as $e^{i\xi(x,y)}|RCP\rangle$ or $e^{i\zeta(x,y)}|LCP\rangle$. Since the rotation of the elements can be arbitrary,

ADVANCED
SCIENCE NEWS
www.advancedsciencenews.com

ADVANCED
OPTICAL
MATERIALS
www.advopticalmat.de

$\xi(x, y)$ or $\zeta(x, y)$ is generally neither equal to nor conjugate with $\varsigma(x, y)$ or $\psi(x, y)$.

To find the relationship between the phase profiles of spin states, we start from the Jones matrix of the dielectric element. A general dielectric element can be described by A_{x_r} and A_{y_r}, which are the transmission components along the x_r and y_r axes, and $\varphi_{x_r}(x, y)$ and $\varphi_{y_r}(x, y)$, which are the corresponding phase responses. We require $A_{x_r}(x, y) = A_{y_r}(x, y)$ and $\varphi_{x_r}(x, y) - \varphi_{y_r}(x, y) = \pi$, a widely adopted condition in PB metasurfaces.[27–31] It can be seen that $\varsigma(x, y) = \varphi_{x_r}(x, y) + 2\theta(x, y)$, $\psi(x, y) = \varphi_{x_r}(x, y) - 2\theta(x, y)$, $\xi(x, y) = \varphi_{x_r}(x, y) + 2\theta'(x, y)$ and $\zeta(x, y) = \varphi_{x_r}(x, y) - 2\theta'(x, y)$ (see Note S1, Supporting Information). Here, $\theta(x, y)$ and $\theta'(x, y)$ are orientation distributions for different designs. We can obtain the following equation

$$\varsigma(x, y) + \psi(x, y) = \xi(x, y) + \zeta(x, y) \tag{1}$$

which shows that the sum of phase profiles for the two spin states is conserved before and after rotating the orientation of elements in a metasurface. By taking differential on both sides, Equation (1) becomes

$$\frac{\partial \varsigma(x, y)}{\partial \vec{r}} + \frac{\partial \psi(x, y)}{\partial \vec{r}} = \frac{\partial \xi(x, y)}{\partial \vec{r}} + \frac{\partial \zeta(x, y)}{\partial \vec{r}} \tag{2}$$
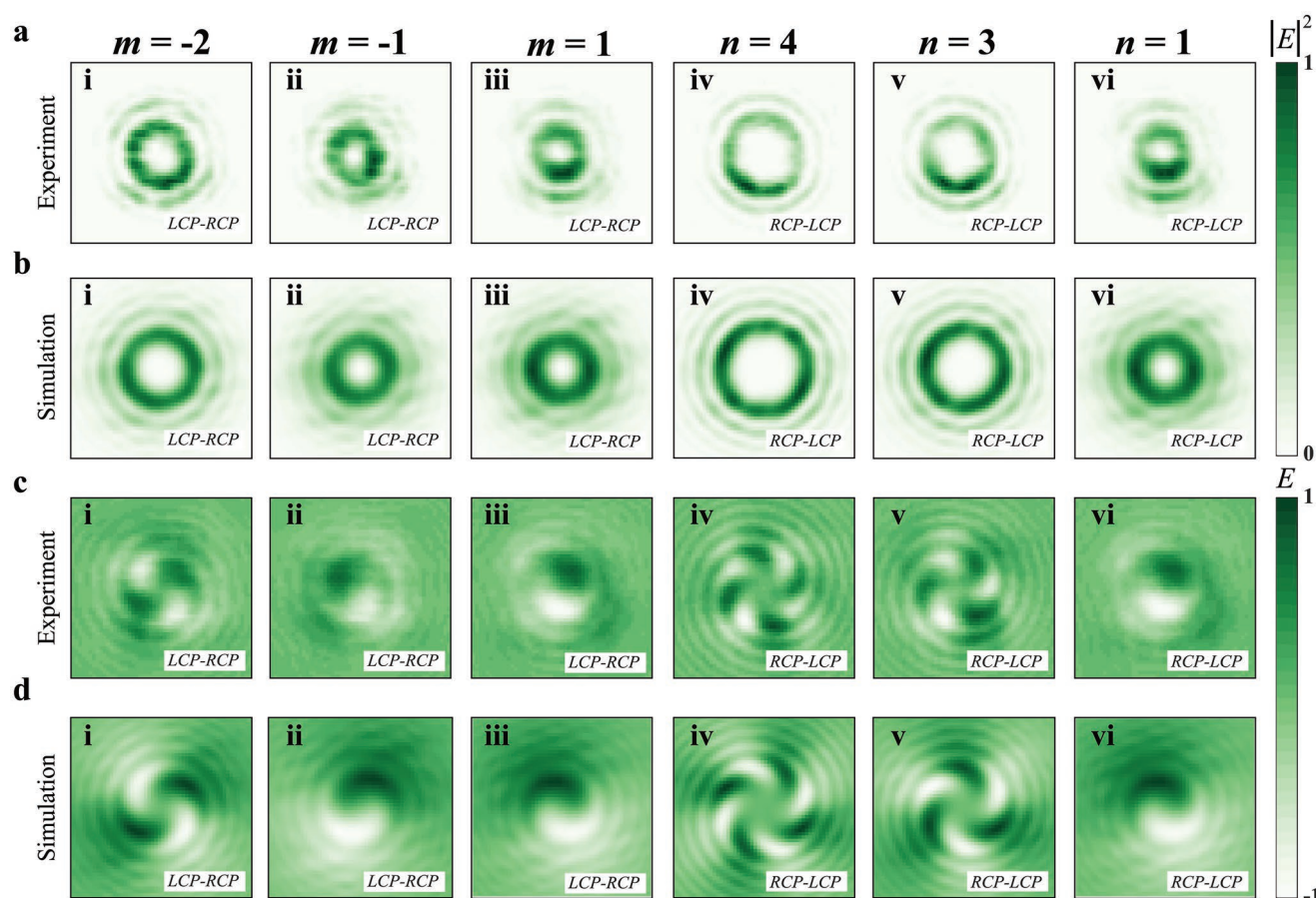
where $\frac{\partial}{\partial \vec{r}}$ represents derivative operator to get the phase gradient, such as $\frac{\partial}{\partial \vec{r}} = \frac{\partial}{\partial x} + \frac{\partial}{\partial y}$. The phase gradient along an interface behaves as a momentum that takes effect in the generalized Snell's law for metasurface designs. It can be found that newly added momenta are conserved for the LCP and RCP in the metasurface before and after rotating the orientation of elements. Equation (2) can provide a guideline of extended spin functionalities that are directly related to phase gradients, such as deflection and orbital angular momentum.

In photonic systems, the conversion of spin angular momentum to orbital angular momentum, refers to the phenomenon in which spin states, i.e., circularly polarized light that carries spin angular momentum, convert to states carrying orbital angular momentum.[30,32–34] We designed metasurfaces that can convert spin angular momentum to different orbital angular momentum by elements' rotation. We denote integer m and n to represent topological charges of the orbital angular momentum of transmitted light in LCP and RCP components, respectively. According to Equation (2), the sum of m and n should be conserved, regardless of assigned orientation distributions. We fabricated the samples by conventional photolithography combined with deep reactive ion etching (see Experimental Section for details). **Figure 2** shows the schematic for constructing versatile phase profiles of spin
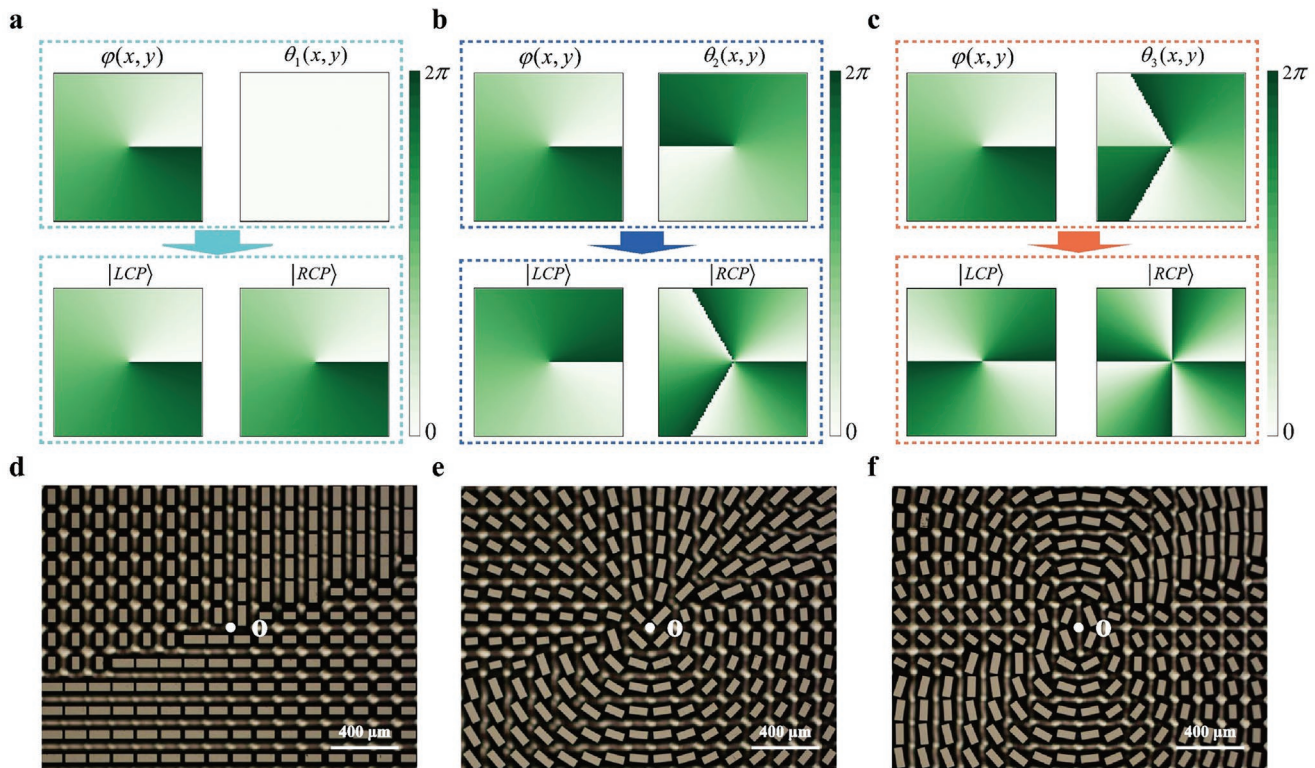
Figure 2. Metasurface designs of versatile orbital angular momentum by rotation of elements. a–c) Schematic of combining a fixed propagation phase with a Pancharatnam–Berry (PB) phase introduced by different orientations of elements. Here, $\varphi(x, y)$ represents the propagation phase of the elements. Combining $\varphi(x, y)$ with $\theta_1(x, y)$ results in $m = -2$ and $n = 4$ for orbital angular momentums of the spin states, respectively. Rearranging orientations to $\theta_2(x, y)$ results in $m = -1$ and $n = 3$, and to $\theta_3(x, y)$ produces $m = 1$ and $n = 1$. d–f) Corresponding optical images of samples. The white dots labeled as "O" in the center show the center of the samples. The scale bar in (d–f) is 400 μm.

**ADVANCED
SCIENCE NEWS**

www.advancedsciencenews.com
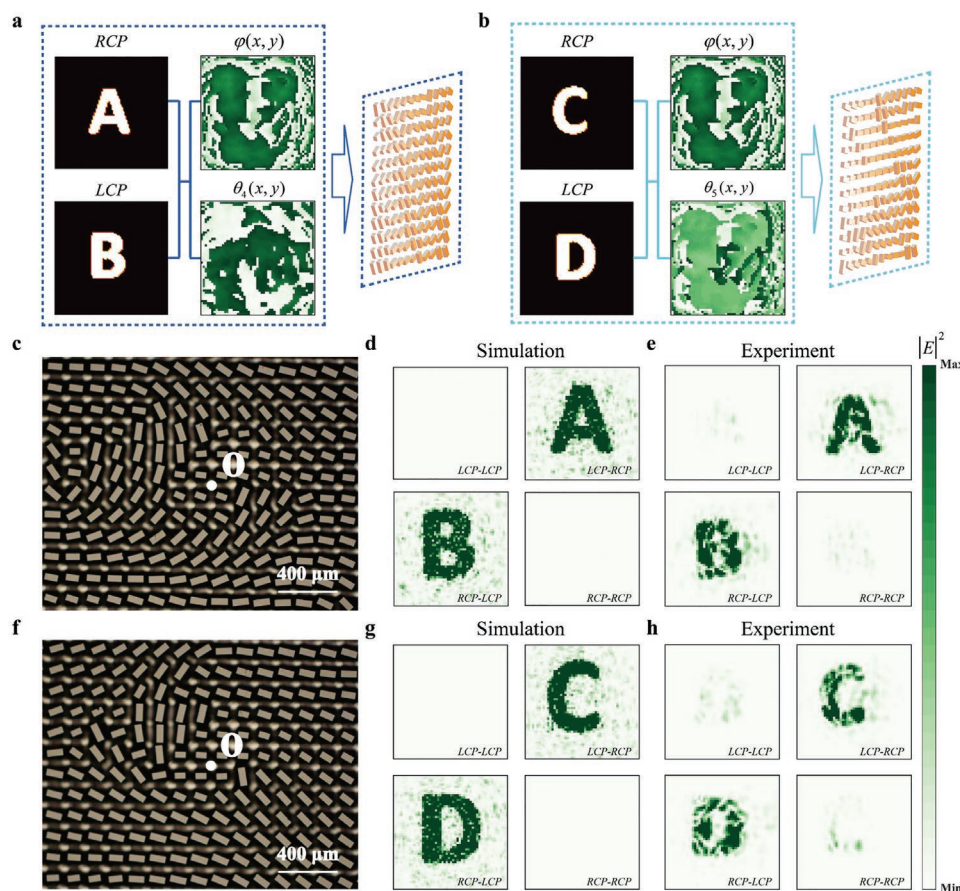
**ADVANCED
OPTICAL
MATERIALS**

www.advopticalmat.de

Figure 3. Demonstration of versatile orbital angular momenta by rotation of elements. a,b) The measured and simulated intensity distributions of the LCP–RCP and RCP–LCP components for the metasurfaces with $\theta_1(x,y)$ (columns i and iv), $\theta_2(x,y)$ (columns ii and v), and $\theta_3(x,y)$ (columns iii and vi), respectively. c,d) The corresponding electric field distributions, respectively.

states by combining a fixed propagation phase with PB phases introduced from different elements' orientations $\theta_i(x,y)$ ($i = 1$, 2, 3). In this design, m is designed to vary from -2, -1 to 1 by using elements' rotation in metasurfaces, while n varies correspondingly from 4, 3 to 1, as shown in Figure 2a–c, respectively. Figure 2d–f shows the partial optical images of corresponding samples, respectively. It can be seen that elements in different samples are identical but differ only in orientation.

The samples were measured by a terahertz field scanning microscope (see Note S2, Supporting Information). **Figure 3** shows the simulated and measured results of the LCP-RCP (LCP component of transmitted light under RCP incidence) and RCP-LCP (RCP component of transmitted light under LCP incidence) components for the metasurfaces with different orientations. Figure 3a,c illustrates the measured intensity and electric field distributions, respectively. The intensity distributions are donut-like patterns that are typical intensity distributions of light carrying orbital angular momentums. The radius of the central donut-like pattern increases as the topological charge of orbital angular momentum increases. These measured results are consistent with the simulations in Figure 3b,d. Different numbers of negative or positive arms, which indicate topological charges of orbital angular momentums, can be distinguished in Figure 3c,d. For example, in Figure 3c,

image i illustrates two positive arms encircling clockwise in the LCP-RCP component, while image iv shows four positive arms encircling counterclockwise, agreeing with the corresponding numerical results in Figure 3d. Consequently, the topological charges are $m = -2$ and $n = 4$ for the metasurface with $\theta_1(x,y)$, as expected. Similarly, the topological charges are $m = -1$ and $n = 3$ for the metasurface with $\theta_2(x,y)$, as shown in images ii and v, and $m = 1$ and $n = 1$ for the metasurface with $\theta_3(x,y)$, indicated by images iii and vi, respectively. It can be seen that the sum of topological charges is conserved.

Now we proceed to demonstrate another class of functionalities, the spin-dependent holograms, which take effect by exhibiting certain distributions of intensity rather than phase. A given hologram or intensity distribution can be reconstructed by different phase profiles. This provides the possibility of switching spin-dependent holograms by the proposed method. Here, we adopted an optimization algorithm that applied the Rayleigh–Sommerfeld diffraction formula as kernel diffraction function and took the phase profile error into the iterative phase update function (see Note S3, Supporting Information). The finite phase profile error violated Equation (1), but it could be optimized to the minimum. As a result, spin-dependent holograms could be switched by rotating elements' orientation in the metasurface.

**ADVANCED
SCIENCE NEWS**

www.advancedsciencenews.com

**ADVANCED
OPTICAL
MATERIALS**

www.advopticalmat.de

Figure 4. Extended spin-dependent holograms by rotation of elements. a) The schematic of encoding letters "A" and "B" to the right-handedness circular polarization (RCP) and left-handedness circular polarization (LCP) components, respectively. $\varphi(x, y)$ and $\theta_4(x,y)$ represent the propagation phase and orientation distribution of the elements, respectively. b) The schematic of encoding letters "C" and "D" to the RCP and LCP component, respectively. $\theta_5(x,y)$ represents the new orientation distribution. c) The optical image of the sample of the metasurface with $\theta_4(x,y)$. d,e) The simulated and measured results for the metasurface with $\theta_4(x,y)$ as in panel a). f) The optical image of the sample of metasurface with $\theta_5(x,y)$. g,h) The simulated and measured results for the metasurface with $\theta_5(x,y)$ as in panel (b). The white dot (c) and (f) represent the reference point. The scale bar in (c) and (f) is 400 μm.

As depicted in **Figure 4**a,b, metasurfaces for spin-dependent holograms are built by the same strategy in Figure 2a–c. The propagation phase $\varphi(x, y)$ and orientation distributions $\theta_i(x,y)$ ($i = 4, 5$) are calculated from the optimized phase distributions for spin-dependent holograms. The letters "A" and "B" are encoded to the LCP and RCP components by combining $\varphi(x, y)$ and $\theta_4(x,y)$, shown in Figure 4a. By rearranging the elements' orientation in the metasurface with $\theta_5(x,y)$, the letters "A" and "B" are switched to letters C" and "D," as illustrated in Figure 4b. Figure 4c,f shows the optical images of samples, which differ only in orientation of elements. The letters "A" and "B" can be distinguished in the measured LCP-RCP and RCP-LCP components in Figure 4e, agreeing well with simulations in Figure 4d. Instead, when the incident spin states interact with the metasurface with $\theta_5(x,y)$, the letters "C" and "D" emerge in both simulations and measurement, as shown in Figure 4g,h. The cross-talk between the LCP-RCP and RCP-LCP components in Figure 4e,h is minimal. Therefore, spin-dependent holograms can be switched by using elements'

rotation in the metasurface. More designs of spin-dependent holograms can be found in Supporting Information.

3. Conclusion

In summary, we have experimentally demonstrated the extended spin functionalities for different spin states in a metasurface by rearranging orientation of elements. The relationship between the phase profiles of spin states before and after the rotation is provided as a guideline for spin functionality design. Terahertz imaging experiment is conducted to observe the conversion from spin angular momentum to different orbital angular momenta. Spin-dependent holograms are designed and characterized to demonstrate the extended spin functionalities before and after the rotation of elements in a metasurface. Although the experiment is performed in the terahertz regime, the design principle is general and can be applied to infrared and visible regimes. We envision that this development can be

useful in applications such as polarization-selective holography and multiplexed spin components in communication.

4. Experimental Section

Material and Fabrication: The silicon is selected due to its low absorption in the terahertz regime, whose refractive index is 3.4. The metasurfaces are fabricated on the 1.5-mm-thick silicon substrate. Fabrication of the metasurface can be classified into three steps: first, the micro-column patterns are defined by E-beam lithography after the silicon wafer is spin-coated with a 10-µm-thick photoresist. Next, deep reactive ion etching is applied to make the silicon pillars with a height of 200 µm. Finally, the silicon wafer is cleaned with acetone solution and DI water.

Characterization and Measurement: The 1550 nm fiber laser with a pulse width of ≈ 50 fs is split into two beams that are used to generate the terahertz radiation and to detect the transmitted terahertz waves, respectively. The terahertz wave is emitted by a commercial photoconductive antenna and then collimated by a TPX terahertz lens. Two metallic grid polarizers are applied to generate and detect different polarization states. The sample is placed between the two metallic grid polarizers. The first polarizer is placed with an orientation of 45° or 135° with respect to the *x*-axis, and the second is placed orthogonal or parallel with the first one. The transmitted light is measured by the commercial terahertz probe. The photoconductive antenna gap of the probe is set along the *x*-axis to detect only the *x* polarized component of the transmitted electric field, which is fixed to detect *x* polarization during the whole experiment (see Note S2, Supporting Information). For example, the linear matrix component t_{xx} is measured by placing the first polarizer with an orientation of 45°, while the second polarized with an orientation of 45°. Then, the linear matrix component t_{xy} is measured by rotating the second polarizer to 135°. The components t_{yy} and t_{yx} are measured similarly. After measuring the linear polarized transmission matrix, it can be transformed to the circularly polarized basis[31]

$$T_{cp}^m = \frac{1}{2}\begin{bmatrix} t_{xx} + t_{yy} + it_{xy} - it_{yx} & t_{xx} - t_{yy} - it_{xy} - it_{yx} \\ t_{xx} - t_{yy} + it_{xy} + it_{yx} & t_{xx} + t_{yy} - it_{xy} + it_{yx} \end{bmatrix} \tag{3}$$

In the measurement, the electric field was scanned with a 0.2 mm step from −5 to 5 mm in both *x*- and *y*- directions. The probe was placed approximately 10 mm above the surface of the sample. The working frequency was shifted to 1.15 THz, which might be due to the shorter etching time that made the height of the pillar being smaller than designed. The measured intensity distributions of the holograms were not as uniform as those of the calculated results, which may be attributed to various imperfections in fabrication and measurement.

Numerical Simulation: The response of the dielectric pillar is simulated in the CST Microwave Studio (Computer Simulation Technology GmbH, Darmstadt, Germany). In the simulation, the periodic boundary condition is applied in both the *x*- and *y*- directions. The open boundary condition is applied in the *z*-direction. The period of the element along the *x*- and *y*- direction is 140 µm. The height of the element is 200 µm. The amplitude and phase responses are acquired by sweeping length *a* and width *b* of the element at 1 THz under *x*- and *y*- polarized incidence, respectively (see Figure S1, Supporting Information). To meet the simplification condition, the elements are selected by the criterion $\Delta A \leq 0.05, A_{x_r} > 0.7$ and $|\varphi_{x_r}(x,y) - \varphi_{y_r}(x,y)| \leq \pi \pm \pi / 36$ (see Table S1, Supporting Information). The metasurfaces are composed of 80×80 elements. The electric field distributions are calculated with the home-built Matlab codes. The Rayleigh–Sommerfeld diffraction formula in the main text is as follows:

$$U(x_0, y_0) = \frac{1}{i\lambda} \iint U(x,y) \cos\langle \mathbf{n}, \mathbf{r} \rangle \frac{\exp(ikr)}{r} dx dy \tag{4}$$

where $U(x_0, y_0)$ and $U(x, y)$ are the electric fields on the image plane and the object plane, respectively. λ and k are the working wavelength and wave number in vacuum, respectively. r is the distance between the pixel in the image plane and that in the object plane: $r = \sqrt{(x_0 - x)^2 + (y_0 - y)^2 + z^2}$; $\cos\langle \mathbf{n}, \mathbf{r} \rangle = \frac{z}{r}$ is the inclination factor.

Supporting Information

Supporting Information is available from the Wiley Online Library or from the author.

Conflict of Interest

The authors declare no conflict of interest.

Data Availability Statement

The data that support the findings of this study are available from the corresponding author upon reasonable request.

[1] N. Yu, P. Genevet, M. A. Kats, F. Aieta, J. P. Tetienne, F. Capasso, Z. Gaburro, *Science* **2011**, *334*, 333.
[2] A. V. Kildishev, A. Boltasseva, V. M. Shalaev, *Science* **2013**, *339*, 1232009.
[3] L. Cong, W. Cao, X. Zhang, Z. Tian, J. Gu, R. Singh, J. Han, W. Zhang, *Appl. Phys. Lett.* **2013**, *103*, 171107.
[4] X. Ni, V. K. Alexander, M. S. Vladimir, *Nat. Commun.* **2013**, *4*, 2807.
[5] C. Pfeiffer, A. Grbic, *Phys. Rev. Appl.* **2014**, *2*, 044012.
[6] W. T. Chen, A. Y. Zhu, F. Capasso, *Nat. Rev. Mater.* **2020**, *5*, 604.
[7] J. Zhou, Q. Wu, J. Zhao, C. Posner, M. Lei, G. Chen, J. Zhang, Z. Liu, *Phys. Rev. Lett.* **2022**, *129*, 020801.
[8] M. V. Berry, *J. Mod. Opt.* **1987**, *34*, 1401.
[9] S. Pancharatnam, S. Pancharatnam, *Resonance* **2013**, *18*, 387.
[10] Z. E. Bomzon, G. Biener, V. Kleiner, E. Hasman, *Opt. Lett.* **2002**, *27*, 1141.
[11] L. Huang, X. Chen, HolgerM. , G. Li, B. Bai, Q. Tan, G. Jin, T. Zentgraf, S. Zhang, *Nano Lett.* **2012**, *12*, 5750.
[12] D. Lin, P. Fan, E. Hasman, M. L. Brongersma, *Science* **2014**, *345*, 298.

**ADVANCED
SCIENCE NEWS**

www.advancedsciencenews.com

**ADVANCED
OPTICAL
MATERIALS**

www.advopticalmat.de

[13] X. Ding, F. Monticone, K. Zhang, L. Zhang, D. Gao, S. N. Burokur, A. Lustrac, Q. Wu, C. W. Qiu, A. Alù, *Adv. Mater.* **2015**, *27*, 1195.

[14] X. Yin, T. Steinle, L. Huang, T. Taubner, M. Wuttig, T. Zentgraf, H. Giessen, *Light: Sci. Appl.* **2017**, *6*, e17016.

[15] P. Berto, L. Philippet, J. Osmond, C. F. Liu, A. Afridi, M. M. Marques, B. M. Agudo, G. Tessier, R. Quidant, *Nat. Photonics* **2019**, *13*, 649.

[16] P. Yu, J. Li, S. Zhang, Z. Jin, G. Schütz, C. W. Qiu, M. Hirscher, N. Liu, *Nano Lett.* **2018**, *18*, 4584.

[17] S. Malek, H.-S. Ee, R. Agarwal, *Nano Lett.* **2017**, *17*, 3641.

[18] N. Nookala, J. Lee, M. Tymchenko, J. S. Gomez-Diaz, F. Demmerle, G. Boehm, K. Lai, G. Shvets, M.-C. Amann, A. Alù, M. Belkin, *Optica* **2016**, *3*, 283.

[19] W. Ye, F. Zeuner, X. Li, B. Reineke, S. He, C. W. Qiu, J. Liu, Y. Wang, S. Zhang, T. Zentgraf, *Nat. Commun.* **2016**, *7*, 11930.

[20] J. Zhang, X. Wei, I. D. Rukhlenko, H. T. Chen, W. Zhu, *ACS Photonics* **2019**, *7*, 265.

[21] J. Li, P. Yu, S. Zhang, N. Liu, *Nat. Commun.* **2020**, *11*, 3574.

[22] Y. Zhang, C. Fowler, J. Liang, B. Azhar, M. Y. Shalaginov, S. Deckoff-Jones, S. An, J. B. Chou, C. M. Roberts, V. Liberman, M. Kang, C. Ríos, K. A. Richardson, C. Rivero-Baleine, T. Gu, H. Zhang, J. Hu, *Nat. Nanotechnol.* **2021**, *16*, 661.

[23] J. Karst, M. Floess, M. Ubl, C. Dingler, C. Malacrida, T. Steinle, L. Ludwigs, M. Hentschel, H. Gissen, *Science* **2021**, *374*, 612.

[24] X. Liu, Q. Wang, X. Zhang, H. Li, Q. Xu, Y. Xu, X. Chen, S. Li, M. Liu, Z. Tian, C. Zhang, C. Zou, J. Han, W. Zhang, *Adv. Opt. Mater.* **2019**, *7*, 1900175.

[25] J. Guo, G. Xu, D. Tian, Z. Qu, C. W. Qiu, *Adv. Mater.* **2022**, *34*, 2201093.

[26] Q. Xu, X. Su, X. Zhang, L. Dong, L. Liu, Y. Shi, Q. Wang, M. Kang, A. Alù, S. Zhang, J. Han, W. Zhang, *Adv. Photonics* **2022**, *4*, 016002.

[27] J. B. Mueller, N. A. Rubin, R. C. Devlin, B. Groever, F. Capasso, *Phys. Rev. Lett.* **2017**, *118*, 113901.

[28] R. C. Devlin, A. Ambrosio, N. A. Rubin, J. B. Mueller, F. Capasso, *Science* **2017**, *358*, 896.

[29] P. Huo, C. Zhang, W. Zhu, M. Liu, S. Zhang, S. Zhang, L. Chen, H. J. Lezec, A. Agrawal, Y. Lu, T. Xu, *Nano Lett.* **2020**, *20*, 2791.

[30] Y. Xu, H. Zhang, Q. Li, X. Zhang, Q. Xu, W. Zhang, G. Hu, X. Zhang, J. Han, W. Zhang, *Nanophotonics* **2020**, *9*, 3393.

[31] Y. Xu, Q. Li, X. Zhang, M. Wei, Q. Xu, Q. Wang, H. Zhang, W. Zhang, C. Hu, Z. Zhang, C. Zhang, X. Zhang, J. Han, W. Zhang, *ACS Photonics* **2019**, *6*, 2933.

[32] Y. Zhao, J. S. Edgar, G. D. Jeffries, D. McGloin, D. T. Chiu, *Phys. Rev. Lett.* **2007**, *99*, 073901.

[33] G. Li, M. Kang, S. Chen, S. Zhang, E. Y. B. Pun, K. W. Cheah, J. Li, *Nano Lett.* **2013**, *13*, 4148.

[34] X. Ouyang, Y. Xu, M. Xian, Z. Feng, L. Zhu, Y. Cao, S. Lan, B.-O. Guan, C. W. Qiu, M. Gu, X. Li, *Nat. Photonics* **2021**, *15*, 901.

2201975 (7 of 7)